KSME

Springer

Journal of Mechanical Science and Technology 34 (10) 2020

Original Article
DOI 10.1007/s12206-020-0920-y

Keywords:
· Cradle type five-axis machine tool
· SSO-ANN
· Thermal error compensation
· Temperature sensitive points
· ‘S’-shaped test piece

Correspondence to:
Yongchao Liu
847439536@qq.com

Citation:
Huang, Z., Liu, Y., Du, L., Yang, H. (2020). Thermal error analysis, modeling and compensation of five-axis machine tools. Journal of Mechanical Science and Technology 34 (10) (2020) 4295~4305.
http://doi.org/10.1007/s12206-020-0920-y

Received August 14th, 2019
Revised July 9th, 2020
Accepted August 4th, 2020

† Recommended by Editor
Yong Tae Kang

Thermal error analysis, modeling and compensation of five-axis machine tools

Zhi Huang[1], Yongchao Liu[1], Li Du[1] and Han Yang[2]

[1]School of Mechanical and Electrical Engineering, University of Electronic Science and Technology of China, Chengdu 611731, China, [2]Sichuan Chengfei Integration Technology Corp., Chengdu 610091, China

Abstract The role of five-axis CNC machine tools (FAMT) in the manufacturing industry is becoming more and more important, but due to the large number of heat sources of FAMT, the thermal error caused by them will be more complicated. To simplify the complicated thermal error model, this paper presents a new modelling method for compensation of the thermal errors on a cradle-type FAMT. This method uses artificial neural network (ANN) and shark smell optimization (SSO) algorithm to evaluate the performance of FAMT, and developing the thermal error compensation system, the compensation model is verified by machining experiments. Generally, the thermal sensitive point screening is performed by a method in which a large number of temperature sensors are arranged randomly, it increases the workload and may cause omission of the heat sensitive point. In this paper, the thermal imager is used to screen out the temperature sensitive points of the machine tool (MT), then the temperature sensor is placed at the position of the heat sensitive point of the FAMT, and the collected thermal characteristic data is used for thermal error modeling. The C-axis heating test, spindle heating test, and the combined movement test are applied in this work, and the results show that the shark smell optimization artificial neural network (SSO-ANN) model was compared to the other two models and verified better performance than back propagation artificial neural network (BP-ANN) model and particle swarm optimization neural network (PSO) model with the same training samples. Finally, a compensation experiment is carried out. The compensation values, which was calculated by the SSO-ANN model are sent to the real-time error compensation controller. The compensation effect of the model is then tested by machining the ‘S’-shaped test piece. Test results show that the 32 % reduction in machining error is achieved after compensation, which means this method improves the accuracy and robustness of the thermal error compensation system.

1. Introduction

In recent years, driven by requirements of aerospace industry, the FAMT has become more and more important in industrial applications for precise manufacturing of complex workpieces. However, the heat sources inside the machine structure (such as ball screw, bearing, shaft driven motor) and environmental temperature changes [1] cause thermal deformation of machine parts. And these thermal errors account for more than 60 % of the total machining error of the CNC FAMT [2], especially the rotating axis (C-axis) of the cradle FAMT. Different from the machine of main spindle, the cooling and heat dissipation characteristics of this type of turntable behave poorly, which make thermal error more serious. Therefore, the unsatisfactory cooling and heat dissipation characteristics bring an unpredictable impact on the machining accuracy of FAMT.

To improve this problem, researchers have employed various methods in modelling the thermal characteristics such as a finite element method [3], finite difference method [4] and finite difference element method [5, 6]. These methods can be used to analyze the heating and the thermal deformation of MT structures. However, the establishment of numerical models could be a great challenge because of the problems of boundary conditions and accurate acquisition of heat transfer characteristics. Therefore, for the successful application of this technology, it is still necessary to test the MT to calibrate the model.

However, contemporary techniques which apply empirical models, are based on experimental measurements of the MT rather than existing models calibration. The thermal errors of MT are predicted by different models including multiple linear regression (MLR) [7], types of back propagation artificial neural networks (BP-ANN) [8], fuzzy logic [9], grey system theory [10] and the combination of different modelling methods.

Miao et al. [11] made use of a combination of fuzzy clustering, gray correlation, stepwise regression, and determination coefficient to optimize temperature measuring points. Then the method is verified on the CNC machining center, the results showed that the temperature measurement points number was reduced from 10 to 2, showing a better prediction results. Besides stronger robustness were achieved under different spindle speeds and ambient temperature conditions. In order to analyze the influence of different heat sources on the thermal error of the spindle, Guo [12] proposed a new ABC-NN (artificial bee colony-based neural network) modeling method to predict the thermal deformation of the spindle, through experimental verification showed that the prediction accuracy of the LSR and ANN models was lower than that of ABC-NN. Abdulshahed et al. [13] proposed a new thermal error compensation modeling method on a FAMT. The method used a grey neural network model with convolution integral (GNNMCI (1, N)), and particle swarm optimization (PSO) algorithm was also used to optimize the proposed GNNMCI (1, N), the Z-axis and C-axis separate movement and combined movement are considered in this experiment, and test results showed that the thermal deformation after compensation was reduced by 85 %. Blaser et al. [14] applied a system of differential equations to calculate the model based compensation values. Based on the changes in the environment temperature, power changes and boundary conditions, the method can predict thermal deformation of the tool center point (TCP). The experimental results showed that the adaptive learning control (ALC) performed better in long-term prediction accuracy for thermal errors. Gebhardt et al. [15] presented a phenomenological compensation model. The thermal error is compensated according to different input powers. The experimental results show that the method can reduce the position error by 70 %. A high-precision gray box model [9] was also proposed for predicting errors caused by internal heat sources such as drives or bearings. This model allowed the TCP error to be corrected based on internal signals, and the model was compensated with a thermal error reduction of 85 %. Du et al. [16] proposed a natural exponential model (NEM) to predict thermal deformation at random rotational speeds, without thermal sensors, and then determine two important parameters. A verification experiment of thermal error at random speed was performed. The results showed that axial thermal error and radial thermal error were reduced by 73 % and 63 %, respectively. Mareš et al. [17] improved the model proposed by predecessors [18] which introduced the spindle power parameter to this model, and modeled the thermal deformation of the spindle under cutting. After testing, thermal error was reduced by 50 %. In the above research, a key issue is the rigor of the number and position of the thermal sensors. The previous methods have a certain blindness when screening temperature sensitive points, and some heat sources are missed, which affects the prediction accuracy of the thermal error model. Another key issue is the speed of model establishment. The previous models are more complex, require more training samples, and have longer training time. When the thermal error is compensated, the prediction difficulty is greatly increased and the real-time compensation control is affected.

In the research of thermal error compensation, the commonly used methods are the origin drift method [19] and the feedback interruption method [20]. Since the original displacement method does not affect the workpiece coordinates and part processing, and the reliability is high, many scholars use this method for thermal error compensation. In the compensation process, it is generally carried out in three steps. At first, the temperatures, the spindle thermal error and other related parameters are measured by kinds of sensors. The gathered signals are processedwith the signal processing unit. Then the data are sent to the PC through the serialport for establishing the spindle thermal error model based on proper methods introduced. By using the PC, the thermal errors are predicted and sent to the PLC as the compensation value through the I/O port [21]. The CNC controller receives the signals form PLC's I/O ports at every compensation interval and the compensation is finally achieved by modifying the motion command of the servo control system or shifting the origin coordinates.

In order to improve the prediction accuracy and efficiency of the model, and improve the machining accuracy of the FAMT. This paper have designed predict thermal errors modelling method and develops a thermal deformation compensation system for the cradle-type FAMT. In order to avoid arranging a large number of temperature sensors blindly, the thermal imaging instrument is firstly used to find the thermal sensitive points that affect the FAMT. Secondly, a temperature sensor is placed at the sensitive temperature point to collect the data of temperature and thermal error. Thirdly, SSO algorithm is used to train the neural network and establish the thermal error prediction model. By comparing and analyzing the BP-ANN model and PSO-ANN neural network model, this model has high thermal error modeling accuracy and speed. Finally, the ‘S’-shaped test piece machining compensation experiment was carried out. Experiment results show that a 32 % reduction in the thermal errors of Z-direction was achieved after compensation. This prediction method improves the machining accuracy of FAMT effectively.

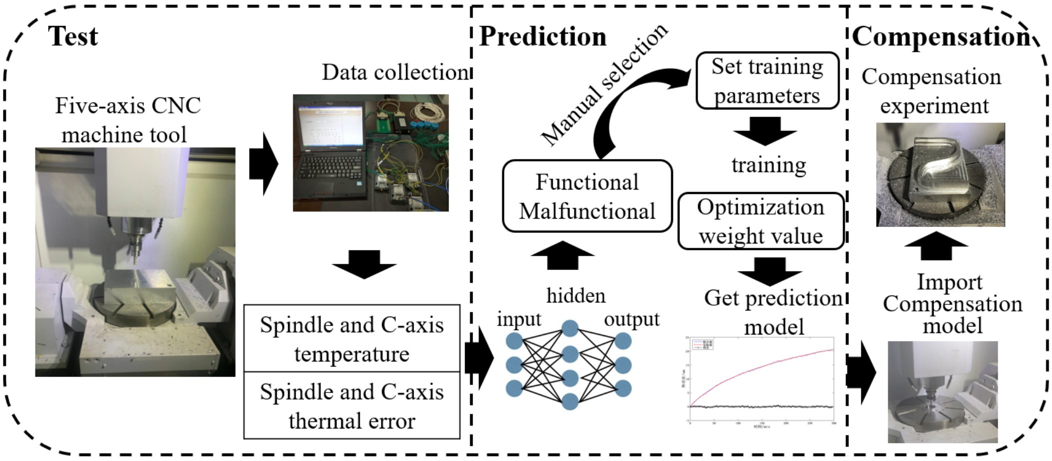

Fig. 1. Prediction and compensation system for five-axis CNC machine tools based on SSO-ANN.

2. Materials and methods

ANN has good data parallel processing capability, storage capacity and data fault tolerance. After appropriate training methods, it can be applied to nonlinear system modeling, prediction and control. Data acquired by the FAMT collection system is normalized and input into the ANN. The output of the ANN is the thermal error of a five-axis CNC machine tool based on the processing performance of the FAMT. Therefore, the ANN can intelligently evaluate the performance of the FAMT after training. Shark smell optimization (SSO) algorithm is a multi-dimensional optimization method, which has been successfully applied to training feedforward neural network [22] and this algorithm is superior to traditional BP training method and PSO training method in prediction accuracy and modeling-speed. Therefore, this paper intends to use the SSO algorithm to train the aforementioned neural network. After training, the neural network can quickly predict the thermal deformation of FAMT and implement the related thermal error compensation control. The specific SSO optimization neural network predicts the thermal error and compensation principle of the FAMT is illustrated in Fig. 1 [23].

2.1 SSO algorithm

The SSO algorithm [24] is derived from the intelligent behavior of sharks hunting based on their strong sense of smell. Sharks are one of the most famous and excellent hunters in nature. The reason for this hunting advantage is the shark's ability to find prey in a short search time with its strong sense of smell in a large search space. The steps of the SSO intelligent algorithm are as follows:

Step 1: Looking for the first scent particles: when the shark smells the prey, the hunting process begins. Actually, the smell is from the injured prey. In order to model the process, an initial solution is randomly generated for the optimization problem in the feasible search space. Each solution represents an odor that represents the possible location of the shark during the hunt.

$$\left[x_1^1, x_2^1, x_3^1, \ldots, x_{NP}^1\right] \tag{1}$$

where x_i^1 represents the ith initial position of the optimization problem, and NP is the size of the group. The optimization problem can be expressed as:

$$x_1^1 = \left[x_{(i,1)}^1, x_{(i,2)}^1, \ldots, x_{(i,ND)}^1\right] i = 1, 2, \ldots, NP \tag{2}$$

where $x_{(i,j)}^1$ = jth dimension of the shark's ith position, and *ND* = number of decision variables.

Step 2: Sharks move toward prey: sharks at each location move at a certain speed and approach the prey. According to the position vector, the initial velocity vector can be expressed as:

$$\left[V_1^1, V_2^1, \ldots, V_{NP}^1\right]. \tag{3}$$

In Eq. (3), the velocity vector has components in each dimension and can be expressed as:

$$V_i^1 = \left[V_{(i,1)}^1, V_{(i,2)}^1, \ldots, V_{(i,ND)}^1\right]. \tag{4}$$

The shark follows the smell of the prey, and its direction of movement changes as the intensity of the scent changes. As the intensity of the odor increases, the speed of the shark also increases. From an optimization point of view, the motion is mathematically represented by the gradient of the objective function. The gradient indicates the direction of acceleration increase. Eq. (5) shows the process:

$$\begin{cases} V_i^k = \eta_k \cdot R_1 \cdot \nabla(OF)\Big|_{(x_i^k)} \\ i = 1, \ldots, NP \quad k = 1, \ldots, k_{\max} \end{cases} \tag{5}$$

where V_i^k = velocity of the shark which is approximately constant; *OF* = objective function, ∇ = gradient of the objective function, $k_{\max}$ = maximum number of stages for forward movement of the shark; *k* = number of stage, η_k = a value in the interval [0,1], and R_1 = a random value which is uniformly distributed in the interval [0,1]. The velocity in each dimension can be calculated by Eq. (6):

$$V_{(i,j)}^{k} = \eta_k \cdot R_1 \cdot \frac{\partial OF}{\partial x_j}\bigg|_{(x_{(i,j)}^{k})} \tag{6}$$

where $i = 1, \ldots, NPj = 1, \ldots, ND \quad k = 1, \ldots, k_{\max}$.

Due to the existence of inertia, acceleration of the shark is limited and its velocity depends on its previous velocity. This process is modeled by a modified Eq. (6) as follows:

$$V_{(i,j)}^{k} = \eta_k \cdot R_1 \cdot \frac{\partial OF}{\partial x_j}\bigg|_{(x_{(i,j)}^{k})} + \alpha_k \cdot R_2 \cdot V_{(i,j)}^{(k-1)} \tag{7}$$

where α_k rate of momentum or inertia coefficient that has a value in the interval of [0,1] and becomes a constant for stage k; and R_2 = random number generator with a uniform distribution on the interval [0,1]. Due to forward movement of the shark, its new position Y_i^{k+1} is determined based on its previous position and velocity:

$$Y_i^{(k+1)} = X_i^k + V_i^k \cdot \Delta t_k \tag{8}$$

where Δt_k = time interval of stage k.

Step 3: The shark changes the search direction by rotating. In addition to forward hunting, the shark also has a rotational motion in its direction to find stronger odor particles. And the rotational motion of the shark proceeds along the closed contour. From an optimization perspective, in order to find better prey, the shark will perform a local search at each stage:

$$Z_i^{(k+1,m)} = Y_i^{(k+1)} + R_3 \cdot Y_i^{(k+1)} \qquad m = 1, \ldots, M \tag{9}$$

where $Z_i^{(k+1,m)}$ = position of point m in the local search, R_3 = a random number with a uniform distribution in the interval [−1, 1], M = number of points in the local search of each stage.

2.2 SSO algorithm optimizes neural network

In this study, the ANN structure contains two hidden layers. Data from a FAMT is acquired by the collection system and manually tagged to generate a training data set. Through the training and testing, the established ANN prediction model realizes the simulation of the machine tool thermal error system, reflecting the change law between temperature change and thermal deformation. The algorithm used to calculate the output thermal deformation value of the ANN is:

$$z_k = \begin{cases} \sum_{i=1}^{J_{k-1}} \omega_{(k,i)} \cdot t_{(k-1,i)} + b_k \\ t_{(k,j)} = ft(z_k) \end{cases} \tag{10}$$

where $\omega_{(k,i)}$ are weights, b_k is bias, fa is the activation function $t_{(k-1,i)}$ are the temperature variables, z_k are the thermal error.

The shark olfactory optimization algorithm used in this paper is used to train the neural network, which can reduce the training time and improve the prediction accuracy. The predicted thermal error data is applied to the thermal error modeling and can be further implemented to implement real-time compensation. The flow of the optimization method is shown in Fig. 2.

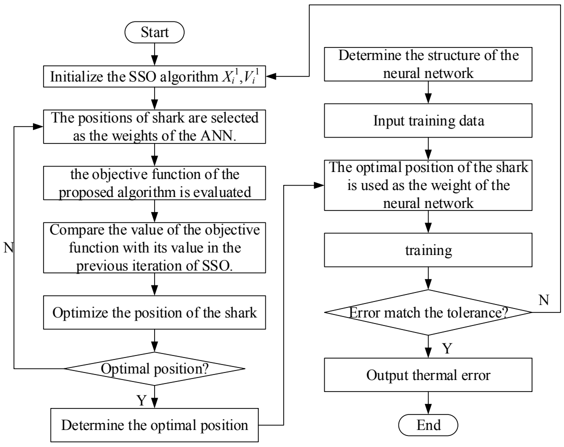

Fig. 2. The flow chart of SSO-ANN algorithm.

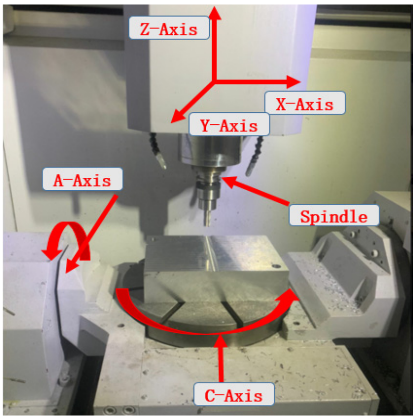

Fig. 3. The configuration of a five-axis machine tool considered in this paper.

3. Experimental setup and approach

In this research, the MT under study was a five-axis cradle milling machine as shown in Fig. 3. The FAMT was constructed of three linear axes X, Y, Z, and two rotary axes (A and C). The maximum speeds along the X/Y/Z axis of the machining center are 20 m/min, 20 m/min, and 20 m/min, and

Fig. 4. Spindle temperature measuring with infrared camera.

Fig. 5. Surface prepared with adhesive tape.

Table 1. Location of thermal sensors on the machine.

Temperature sensor number	Installation location
T1	Spindle bearing
T2	Spindle inner casing
T3	Spindle housing
T4	Ambient temperature 1
T5	Spindle motor
T6	Rotating table side
T7	Left side of A-axis
T8	Right side of A-axis
T9	C-axis motor
T10	Ambient temperature 2

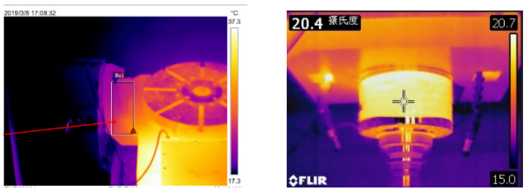

(a) (b)

Fig. 6. Thermal image captured during the experimental: (a) A/C-axis temperature field distribution; (b) spindle temperature field distribution.

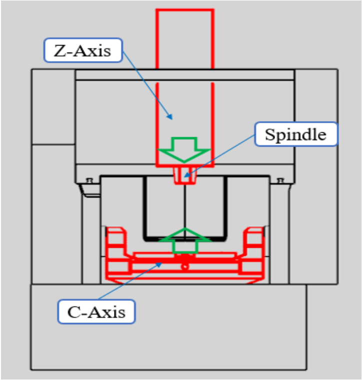

Fig. 7. Schematic diagram of C-axis and A-axis thermal error superposition.

(a) (b)

Fig. 8. Schematic diagram of (a) spindle; (b) C-axis temperature sensor installation.

the travels are 600 mm, 560 mm, and 450 mm, respectively. The maximum speed of the spindle was 8000 rpm. The numerical control system was SIEMENS 840DSL.

The first step in thermal error modeling was to perform an initial evaluation of the FAMT through a thermal imager to identify the FAMT structural components and heat sources that contribute the most to FAMT's error. The thermal imager was applied to record the temperature distribution on the FAMT during the drying operation (in order to stimulate the maximum thermal characteristics of the FAMT's spindle and C-axis, no cooling liquid is used in this article for real-time cooling). In order to reduce the impact of external reflection on the test, the adhesive tape was also attached to the reflective surface of the spindle (see Fig. 5) and turn off the light during the test.

Measuring the distribution of FAMT temperature field by thermal imager (see Fig. 6), the two main causes of thermal deformation were the rotation of the spindle and the C-axis (the thermal error caused by the drilling position is not considered in this paper because the other shafts do not generate significant heat). And the thermal deformation be-tween the two axes produced a super position effect (see Fig. 7), which would make the thermal error more serious. It was the main influencing factor of the thermal error of the FAMT. Therefore, these two axes were analyzed in this paper importantly. A 'virtual' temperature sensor was generated from the thermal image to determine the optimal position to mount the surface mount temperature sensor on the surface of the structure (Fig. 6). Through the preliminary test of FAMT, 8 heat sources were found on the FAMT. 10 temperature sensors were installed on or near the major heat sources (two of the temperature sensors measure the ambient temperature). The installation locations of the 10 temperature sensors were shown in Fig. 8 and Table 1.

Three displacement sensors which were fixed on the fixture,

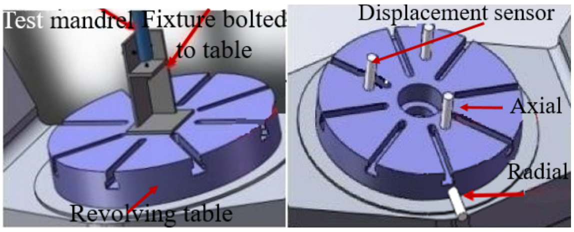

(a) (b)

Fig. 9. Measuring the thermal error of (a) the spindle; (b) C-axis.

were used to measure the displacement of a test mandrel (attached to the spindle) caused by the thermal distortion of the FAMT (see Fig. 9(a)); three displacement sensors measured the thermal error of the C-axis in the axial direction (the average value of measured data was taken as the axial thermal error of C-axis), and one displacement sensor measured the thermal expansion error of the C-axis in the radial direction (see Fig. 9(b)).

4. Experimental setup and approach

4.1 Case 1: spindle heating test and analysis

The spindle was rotated for 4 hours at 8000 r/min, and the thermal error generated by the spindle in the X, Y, and Z directions was tested to obtain the thermal characteristics of the spindle. The temperature variables were measured by the temperature sensors and the displacement sensor was used to measure spindle displacement change. The data was given in Figs. 10 (temperature) and 11 (thermal displacement).

As can be seen in Figs. 10 and 11, when only the spindle was running, the spindle temperature gradually increases with time. Therefore, the thermal error of the spindle in the Z direction increased with the increase of temperature, reaching the steady state at about 3.5 hours. However, after reaching the thermal equilibrium, the temperatures and thermal errors fluctuated in a little range around the equilibrium points. At this time, the thermal error of the spindle in the Z direction could be up to 46 um. Because the thermal error in the X and Y directions does not change much, it can be ignored. Therefore, only the thermal deformation of the spindle in the Z-direction was considered.

4.2 Case 2: C-axis heating test

The C-axis was rotated for 4 hours at 20 r/min, and the thermal error generated by the C-axis in the axial direction and radial direction is tested to obtain the thermal characteristics of the C-axis. The temperature variables were measured by the temperature sensors and the displacement sensor was used to measure spindle displacement change. The data is given in Figs. 10 (temperature) and 11 (thermal displacement).

It can be seen from Figs. 12 and 13. When only the C-axis was running, the temperature inside the C-axis gradually increased with time, and the axial error could reach up to 33 um (because the radial thermal error did not change much, so this paper did not consider it). Although the C-axis speed was low, the C-axis temperature rise and the maximum temperature rise of the high-speed spindle were almost the same. This was due to the poor heat dissipation characteristics of the C-axis, and a large amount of heat was not emitted in the rotary table, resulting in relatively large thermal deformation.

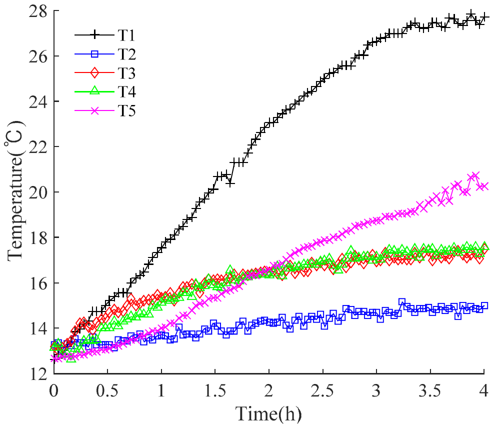

Fig. 10. Temperature variations of 5 heat sources on the spindle.

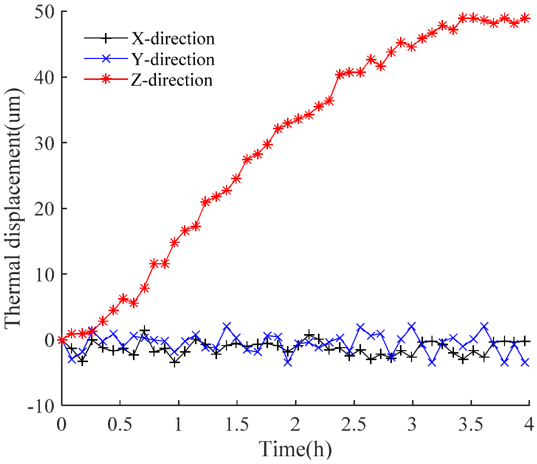

Fig. 11. Thermal displacement of the spindle.

4.3 Case 3: combined axis test

In this test, the C-axis rotated while the spindle rotated simultaneously. The purpose was to verify whether the heat source between the spindle and the C-axis interacted with each other. In this experiment, the spindle (6000 r/min) and the C-axis (20 r/min) were run together for 5 minutes and then stopped for one minute for thermal error measurement. The thermal error in the Z direction when the spindle and the C-axis move together was shown in Fig. 14.

When the spindle and the C-axis moved together, the temperature test results were similar to those in Figs. 10 and 12. Because the distance between the two was far, the temperature between them had little effect. Combined with Figs. 11 and

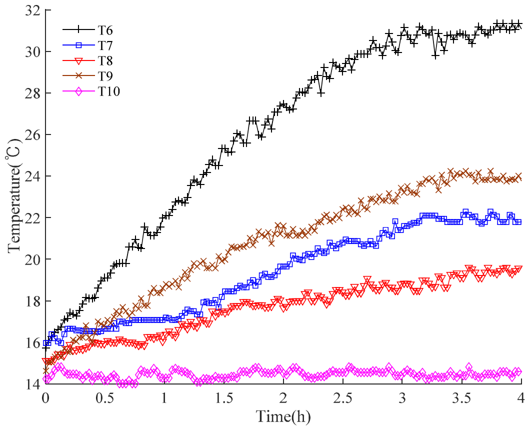

Fig. 12. Temperature variations of 5 heat sources on C-axis.

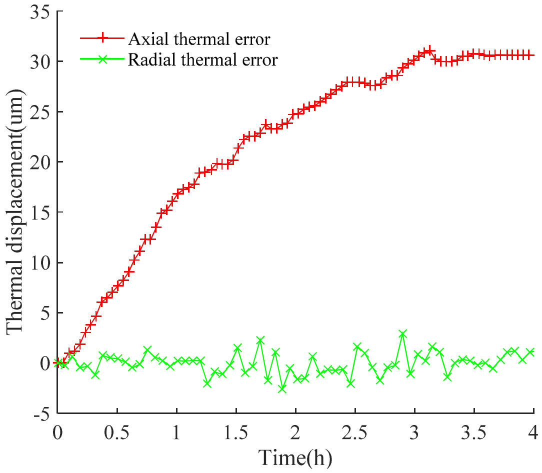

Fig. 13. Thermal drift of the C-axis.

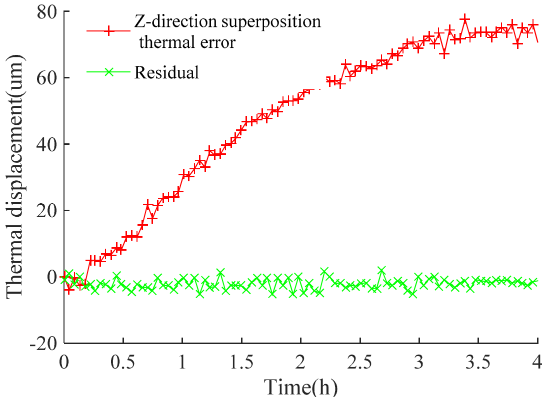

Fig. 14. Thermal error in the Z direction when the spindle and C-axis move together.

Table 2. Performance comparison of spindle thermal error prediction model.

Model	Training time	Performance indices		
		R	RMSE	Residual
BP-ANN	29 s	0.9773	5.12	±8 um
PSO-ANN	21 s	0.9879	3.01	±6 um
SSO-ANN	0.5 s	0.9985	0.83	±3 um

Table 3. Performance comparison of C-axis thermal error prediction model.

Model	Training time	Performance indices		
		R	RMSE	Residual
BP-ANN	25 s	0.9758	3.31	±6 um
PSO-ANN	18 s	0.9886	2.75	±4 um
SSO-ANN	0.5 s	0.9998	0.27	±2 um

Table 4. Cutting process parameters during verification tests.

Workpiece	‘S’-shaped test piece
Texture	Aluminum alloy
Ambient temp.	20 °C
Speed of spindle during rough machining	4000 r/min
Speed of spindle during finishing	6000 r/min
C-axis maximum speed	20 r/min
Roughing time	65 min
Finishing time	27 min

13. It could be seen from the green line in Fig. 14 that the difference between the sum of the thermal errors produced by the two axes of individual motion and the thermal error generated by the linkage was within 10 um or less. It could be concluded that the heat sources of both the main shaft and the C-axis had almost no influence on each other. Therefore, when compensating, the predicted values of the two could be added as compensation values to compensate.

4.4 Comparison with other models

In order to evaluate the performance of SSO-ANN model compared with traditional BP-ANN [8] model and PSO-ANN [13] model, using these three models to predict thermal errors separately, and comparing the predicted values with actual values (see Figs. 15 and 16). The performance indices of three thermal prediction models are given and compared in Tables 4 and 5.

It can be seen from Figs. 15 and 16 that the three methods can accurately predict the thermal error and reduce the residual value of the predicted value to less than 15 um, but the error fluctuations after fitting the first two models are relatively large, and the fitting accuracy is lower.

Combined with Tables 2 and 3, it can be concluded that the SSO-ANN model has smaller root mean square error (RMSE), residual value (residual) and higher correlation coefficient (R) than the other two models, with the same sample size, its modeling accuracy and efficiency are better than the BP-ANN model and the PSO-ANN model.

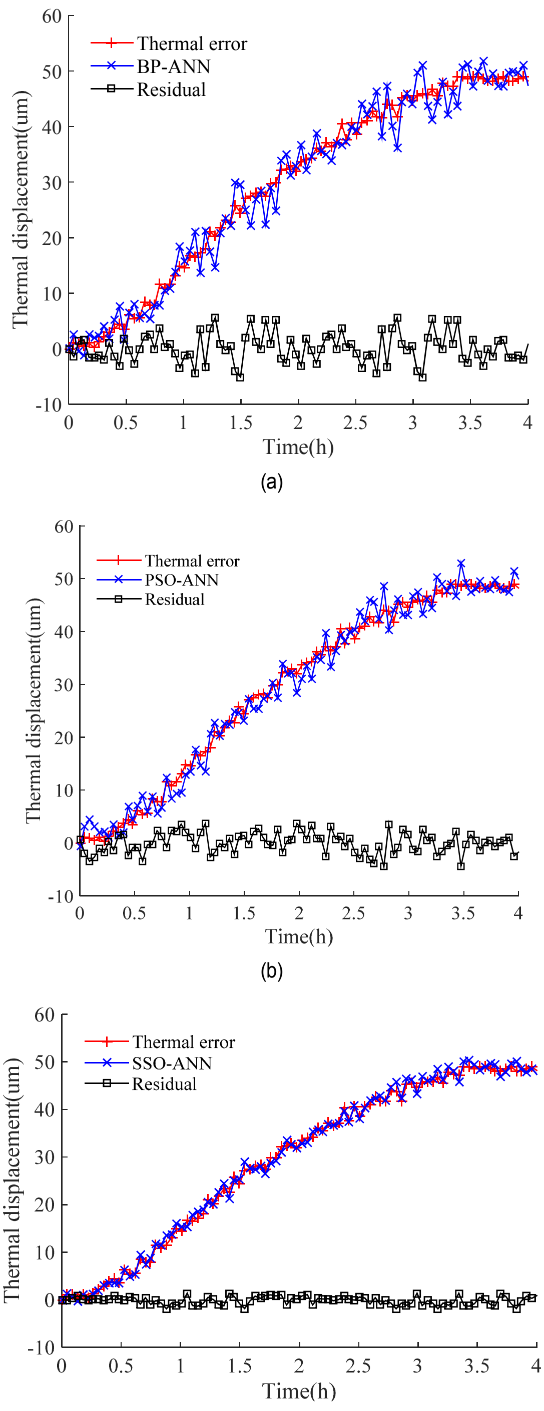

(a)

(b)

(c)

Fig. 15. Spindle thermal error modeling: (a) BP-ANN model output vs. the actual thermal drift; (b) PSO-ANN model output vs. the actual thermal drift; (c) SSO-ANN model output vs. the actual thermal drift.

4.5 Verification of model-based compensation

To validate the SSO-ANN model, the compensation software was developed for the 840DSL CNC system. The thermal error compensation diagram and compensation software interface are shown in Figs. 17 and 18.

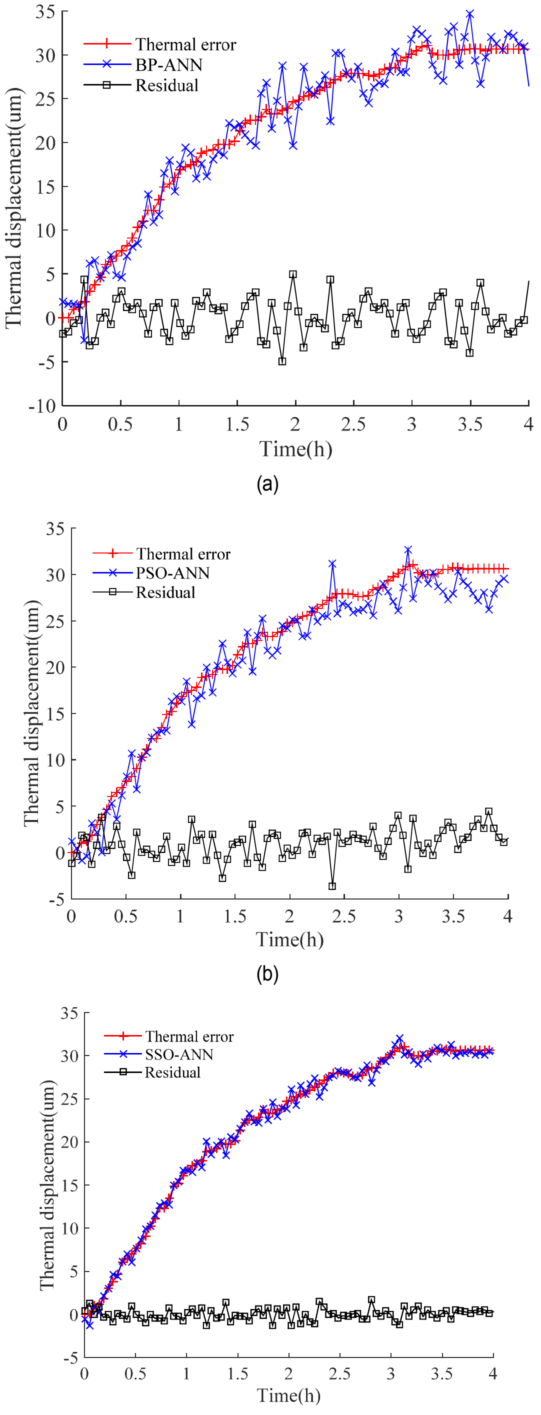

(a)

(b)

(c)

Fig. 16. C-axis thermal error modeling: (a) BP-ANN model output vs. the actual thermal drift; (b) PSO-ANN model output vs. the actual thermal drift; (c) SSO-ANN model output vs. the actual thermal drift.

In order to verify the prediction effect of the model, the compensation experiment of the cradle type FAMT was carried out in the manner of processing the ‘S’-shaped test piece as shown in Fig. 19(a) (because of the the limitation of the experimental conditions, the temperature of the drilling position is

Table 5. No. 1 of ‘S’-shaped test piece measurement data.

Layers	Group	Theoretical position			Error without compensation			Error with compensation		
		X (mm)	Y (mm)	Z (mm)	ΔX (mm)	ΔY (mm)	ΔZ (mm)	ΔX (mm)	ΔY (mm)	ΔZ (mm)
The first layer	1	-130.2508	-70.8527	25.0000	-0.0113	0.0128	0.0437	-0.0081	0.0089	0.0223
	2	-129.2423	-46.1641	25.0000	0.0232	0.0212	-0.0528	0.0189	0.0147	-0.0330
	⋮	⋮	⋮	⋮	⋮	⋮	⋮	⋮	⋮	⋮
	25	114.2947	74.8496	25.0000	0.0117	0.0129	0.0412	0.0095	0.0034	0.0319
The second layer	26	-133.3897	-70.2753	11.0000	0.0215	-0.0211	0.0428	-0.0155	0.0151	0.0235
	27	-132.6081	-45.0232	11.0000	-0.0323	0.0305	0.0637	-0.0063	0.0052	0.0459
	⋮	⋮	⋮	⋮	⋮	⋮	⋮	:	:	:
	50	117.3641	74.2764	11.0000	0.0163	0.0144	0.0512	0.0061	0.0049	0.0334

Table 6. No. 2 of ‘S’-shaped test piece measurement data.

Layers	Group	Theoretical position			Error without compensation			Error with compensation		
		X (mm)	Y (mm)	Z (mm)	ΔX (mm)	ΔY (mm)	ΔZ (mm)	ΔX (mm)	ΔY (mm)	ΔZ (mm)
The first layer	1	-130.2508	-70.8527	25.0000	0.0176	0.0143	0.0384	0.0142	0.0198	0.0186
	2	-129.2423	-46.1641	25.0000	0.0190	-0.0131	0.0424	0.0118	-0.0134	0.0225
	:	:	:	:	:	:	:	:	:	:
	25	114.2947	74.8496	25.0000	0.0132	0.0106	0.0412	0.0103	0.0084	0.0298
The second layer	26	-133.3897	-70.2753	11.0000	-0.0243	0.0228	0.0428	-0.0168	0.0159	0.0218
	27	-132.6081	-45.0232	11.0000	0.0185	0.0113	0.0466	0.0163	0.0092	0.0359
	:	:	:	:	:	:	:	:	:	:
	50	117.3641	74.2764	11.0000	0.0215	0.0144	-0.0450	0.0061	0.0049	-0.0395

Table 7. No. 3 of ‘S’-shaped test piece measurement data.

Layers	Group	Theoretical position			Error without compensation			Error with compensation		
		X (mm)	Y (mm)	Z (mm)	ΔX (mm)	ΔY (mm)	ΔZ (mm)	ΔX (mm)	ΔY (mm)	ΔZ (mm)
The first layer	1	-130.2508	-70.8527	25.0000	0.0213	-0.0128	0.0437	0.0165	-0.0098	0.0185
	2	-129.2423	-46.1641	25.0000	0.0192	0.0212	0.0528	0.0134	0.0118	0.0432
	:	:	:	:	:	:	:	:	:	:
	25	114.2947	74.8496	25.0000	0.0138	0.0129	0.0412	0.0112	0.0121	0.0235
The second layer	26	-133.3897	-70.2753	11.0000	0.0115	0.0211	-0.0428	0.0105	0.0158	-0.0247
	27	-132.6081	-45.0232	11.0000	0.0203	0.0305	0.0637	0.0144	0.0154	0.0502
	:	:	:	:	:	:	:	:	:	:
	50	117.3641	74.2764	11.0000	0.0183	-0.0144	0.0512	0.0161	-0.0089	0.0334

not considered in this experiment). A total of 3 sets (compensated and uncompensated) were carried out in the experiment. Two ‘S’-shaped test pieces were processed in each set of experiments (compensated and uncompensated). Each ‘S’-shaped test piece was processed in three layers. The processing parameters are shown in Table 4. The measurement of the ‘S’-shaped test piece by the coordinate measuring machine (the international standard of ‘S’-shaped test piece [25] only need to measure 2 layers), as shown in Fig. 19(b). The error after uncompensated and compensated is shown in Tables 5-7, which were got by HEXGANO GLOBLE CLASSIC SR.

The error data in the three directions of Tables 5-7 were taken as absolute values and then averaged to obtain the average thermal error of the direction (see Fig. 20).

As can be seen from Fig. 20, the average error in the two directions of X/Y is relatively small, ignoring the influence of thermal error. After compensation, the Z-direction average error was reduced from around 48 um to around 33 um, and the machining accuracy of the ‘S’-shaped test piece was improved by 32 %, which indicated that the thermal error modeling and its compensation method were effective. Although the compensation had some effects, there was still some deviation be-tween the compensation result and the theoretical prediction. One of the reasons was that due to the actual cutting force added during the actual machining process, the components (such as the ball, screw, bearing) were more heated. Another

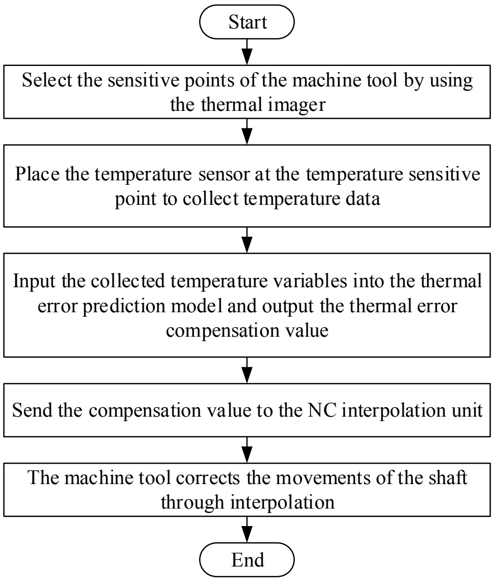

Fig. 17. Thermal error compensation diagram.

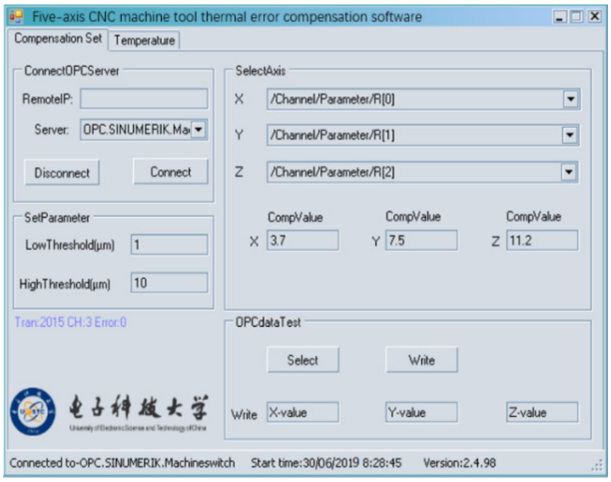
Five-axis CNC machine tool thermal error compensation software

RemoteIP:
Server: OPC.SINUMERIK.Ma
X /Channel/Parameter/R[0]
Y /Channel/Parameter/R[1]
Z /Channel/Parameter/R[2]
LowThreshold(μm) 1
HighThreshold(μm) 10
CompValue X 3.7
CompValue Y 7.5
CompValue Z 11.2
Tran:2015 CH:3 Error:0
Write X-value Y-value Z-value
Connected to-OPC.SINUMERIK.Machineswitch Start time:30/06/2019 8:28:45 Version:2.4.98

Fig. 18. Thermal error compensation software interface.

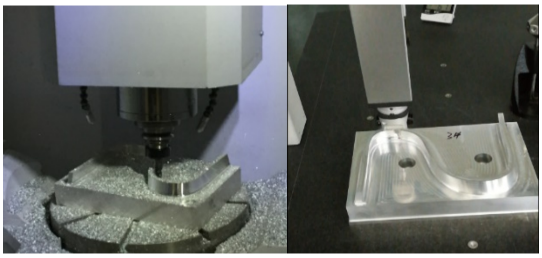
(a) (b)

Fig. 19. (a) Machining test set up; (b) measuring workpiece accuracy.

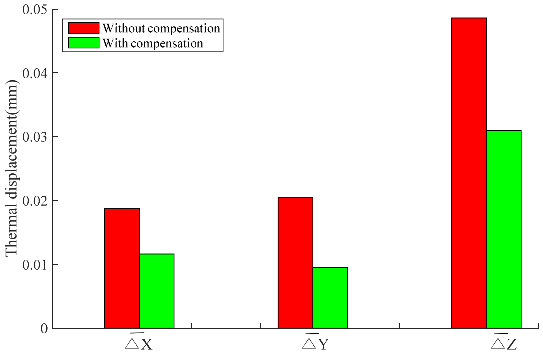

Fig. 20. Comparison of machining accuracy of S-piece without compensation and with compensation.

reason was the introduction of the servo dynamics error of each axis during the S-piece machining process. Therefore, the compensation value in the actual machining process was greater than the predicted value under no-load. These two main reasons led to some differences between the thermal error under no-load and the thermal error in the actual processing state. The next research work can consider further thermal error analysis under different processing conditions.

5. Conclusions

This research work proposed the method of SSO-ANN to predict the thermal error of the cradle FAMT. Base on this method, a compensation system was developed to compensate for the thermal errors. The compensation system had been verified to be high-precision and efficient, and could be used to reduce thermal errors from heating of the spindle and C-axis of a cradle FAMT by over 32 % in the process the ‘S’-shaped test piece test by the compensation model. The proposed model was then compared to BP-ANN model and PSO-ANN and demonstrated a better performance with the same training samples.

In this paper, a non-contact temperature measurement method that using the thermal imager was applied to record the spindle and C-axis temperature distribution. This method was exploited to find the optimal location for temperature measurement and minimize the number of temperature sensors when designing a thermal error prediction model. It can reduce the omission of thermal positioning and improve the scientific positioning of the sensor, further improve the prediction accuracy of the model.

Acknowledgments

This research was supported by National Major Project of China (No. 2017ZX04002001).

Nomenclature

um : Unit of measurement for thermal error
°C : Unit of temperature
mm : Unit of measurement in three coordinates
h,min,s : Unit of time
r/min : Rotate speed

References

[1] Y. Liu, E. Miao and H. Liu, Robust machine tool thermal error compensation modelling based on temperature-sensitive interval segmentation modelling technology, *International Journal of Advanced Manufacturing Technology*, 106 (2) (2020) 655-669.

[2] C. Zhang, F. Gao and Y. Li, Thermal error characteristic analysis and modeling for machine tools due to time-varying environmental temperature, *Precision Engineering*, 47 (1) (2017) 231-238.

[3] J. W. Fan, X. Jia and G. C. Qi, Thermal characteristics analysis of spindle of CNC grinding machine wheel based on ANSYS, *Manufacturing Technology & Machine Tool*, 8 (12) (2019) 55-61.

[4] Z. J. Li, C. Y. Zhao and B. C. Wen, Heat source rate identification and thermal error predictions of ball screw feed drive system for CNC machine tools, *Journal of Northeastern University (Natural Science)*, 40 (9) (2019) 1305-1309.

[5] T. J. Li and K. Liu, Dynamic model on thermally induced characteristics of ball screw systems, *International Journal of Advanced Manufacturing Technology*, 103 (1) (2019) 3703-3715.

[6] Y. Li, W. Zhao and S. Lan, A review on spindle thermal error compensation in machine tools, *International Journal of Machine Tools and Manufacture*, 95 (4) (2015) 20-38.

[7] H. Liu, E. Miao and X. D. Zhuang, Thermal error robust modeling method for CNC machine tools based on a split unbiased estimation algorithm, *Precision Engineering*, 51 (8) (2017) 169-175.

[8] C. Ma, L. Zhao and X. Mei, Thermal error compensation of high-speed spindle system based on a modified BP neural network, *International Journal of Advanced Manufacturing Technology*, 89 (7) (2017) 3071-3085.

[9] A. M. Abdulshahed, A. P. Longstaff and S. Fletcher, Thermal error modelling of machine tools based on ANFIS with fuzzy c-means clustering using a thermal imaging camera, *Applied Mathematical Modelling*, 39 (7) (2015) 1837-1852.

[10] M. Gebhardt, J. Mayr and N. Furrer, High precision grey-box model for compensation of thermal errors on five-axis machines, *CIRP Annals-Manufacturing Technology*, 63 (1) (2014) 509-512.

[11] E. Miao, Y. Y. Gong and L. C. Dang, Temperature-sensitive point selection of thermal error model of CNC machining center, *The International Journal of Advanced Manufacturing Technology*, 74 (5) (2014) 681-691.

[12] Q. Guo, S. Fan and R. F. Xu, Spindle thermal error optimization modeling of a five-axis machine tool, *Chinese Journal of Mechanical Engineering*, 30 (3) (2017) 746-753.

[13] A. M. Abdulshahed, A. P. Longstaff and S. Fletcher, Thermal error modelling of a gantry-type 5-axis machine tool using a grey neural network model, *Journal of Manufacturing Systems*, 41 (10) (2016) 130-142.

[14] P. Blaser, F. Pavliček and K. Mori, Adaptive learning control for thermal error compensation of 5-axis machine tools, *Journal of Manufacturing Systems*, 44 (7) (2017) 302-309.

[15] M. Gebhardt, M. Ess and S. Weikert, Phenomenological compensation of thermally caused position and orientation errors of rotary axes, *Journal of Manufacturing Processes*, 15 (4) (2013) 452-459.

[16] Z. C. Du, S. Y. Yao and J. G. Yang, Thermal behavior analysis and thermal error compensation for motorized spindle of machine tools, *International Journal of Precision Engineering and Manufacturing*, 16 (7) (2015) 1571-1581.

[17] M. Mareš and O. Horejš, Modelling of cutting process impact on machine tool thermal behaviour based on experimental data, *Procedia CIRP*, 58 (8) (2017) 152-157.

[18] O. Horejš, M. Mareš and J. Hornych, A general approach to thermal error modelling of machine *tools, Machines et Usinage à Grande Vitesse (MUGV)*, Clermont Ferrand, France (2014) 1-10.

[19] X. D. Yao, Z. C. Du and G. Y. Ge, Dynamic temperature gradient and unfalsified control approach for machine tool thermal error compensation, *Journal of Mechanical Science and Technology*, 34 (1) (2020) 319-331.

[20] Z. Huang, Z. J. Jia and T. Deng, Thermal error compensation of static pressure turntable based on support vector machine, *Journal of Zhejiang University (Engineering Science)*, 8 (8) (2019) 1594-1601.

[21] A. N. Polyakov and I. V. Parfenov, Thermal error compensation in CNC machine tools using measurement technologies, *Journal of Physics Conference Series*, 1333 (10) (2019) 1-7.

[22] O. Abedinia and N. Amjady, Short-term wind power prediction based on hybrid neural network and chaotic shark smell optimization, *International Journal of Precision Engineering and Manufacturing-Green Technology*, 2 (3) (2015) 245-254.

[23] G. Li, H. Zhou and X. Jing, An intelligent wheel position searching algorithm for cutting tool grooves with diverse machining precision requirements, *International Journal of Machine Tools and Manufacture*, 122 (11) (2017) 149-160.

[24] O. Bozorg-Haddad, *Advanced Optimization by Nature-Inspired Algorithms*, Springer, Singapore (2018).

[25] ISO 10791-7:2014, *Preview Test conditions for Machining Centres Part 7: Accuracy of Finished Test Pieces,* International Organization for Standardization (2014).

Zhi Huang is an Associate Professor in the School of Mechanical and Electrical Engineering of University of Electronic Science and Technology of China. His research areas include advanced grinding technology for difficult-to-machine materials, advanced numerical control equipment, and theory of detection and control technology for complex machining processes. In recent years, he has completed the National Natural Science Foundation of China, national science and technology major projects, etc.